The Buckling Spectra of Nanoparticle Surfactant Assemblies

Joe Forth[1,2], Andres Mariano[1,3], Yu Chai[1,4,5], Anju Toor[1,6], Jaffar Hasnain[1,3], Yufeng Jiang[1,6], Wenqian Feng[1], Xubo Liu[1,9], Phillip Geissler[1,3], Narayanan Menon[7], Brett A. Helms[1,4], Paul D. Ashby[1,4], Thomas P. Russell[8,1,9,10]*

[1]Materials Sciences Division, Lawrence Berkeley National Laboratory, Berkeley, CA 94720, USA

[2]Department of Chemistry, University College London, London, WC1H 0AJ, United Kingdom

[3]Department of Chemistry, University of California, Berkeley, CA 94720, USA

[4]Molecular Foundry, Lawrence Berkeley National Laboratory, Berkeley, CA 94720, USA

[5]Department of Physics, City University of Hong Kong, Hong Kong SAR, China

[6]School of Materials Science and Engineering, University of California, Berkeley, CA 94720, USA

[7]Department of Physics, University of Massachusetts, Amherst, MA, USA

[8]Polymer Science and Engineering Department, University of Massachusetts, 120 Governors Drive, Conte Center for Polymer Research, Amherst, Massachusetts, 01003, USA

[9]Beijing Advanced Innovation Center for Soft Matter Science and Engineering, Beijing University of Chemical Technology, Beijing 100029, China

[10]Advanced Institute for Materials Research (WPI-AIMR), Tohoku, University, 2-1-1 Katahira, Aoba, Sendai 980-8577, Japan

*email: tom.p.russell@gmail.com

Fine control over the mechanical properties of thin sheets underpins transcytosis,[1] cell shape,[2] and morphogenesis.[3] Applying these principles to artificial, liquid-based systems has led to reconfigurable materials for soft robotics,[4] actuation,[5] and chemical synthesis.[6] However, progress is limited by a lack of synthetic two-dimensional membranes that exhibit tunable mechanical properties over a comparable range to that seen in nature. Here, we show that the bending modulus, B, of thin assemblies of nanoparticle surfactants (NPSs) at the oil-water interface can be varied continuously from sub-k_BT to 10^6 k_BT, by varying the ligands and particles comprising the NPS. We find extensive departure from continuum behaviour, including enormous mechanical anisotropy and a power law relation between B and the buckling spectrum width. Our findings provide a platform for shape-changing liquid devices and motivate new theories for the description of thin film wrinkling.[7]

Surface tension drives the assembly of nanoparticles (NPs) at liquid–liquid interfaces.[8] At sufficiently high densities, the NPs solidify into two-dimensional elastic sheets made of discrete building blocks.[9] These solid-like interfaces can be combined with additive manufacturing techniques to produce complex, hierarchical structures made entirely of liquids, such as bicontinuous networks,[10] fibrils,[11] and cellular materials.[12] Combining this morphological control with the enormous palette of functional nanomaterials that can now be synthesized has led to novel platforms for cell culture,[13] microfluidics,[14] and synthetic biology.[15] In these interface-rich materials, structure is determined by a balance between surface tensions, adhesion energies, and the mechanical moduli of the oil-water interface.[16] Fine control of these moduli inherently leads to shape control and actuation, allowing for the development of all-liquid, 4D printed materials.[17] At the same time, dimensionally confined assemblies of NPs offer a system for

testing the breakdown of continuum theories in nanoscale, granular, or high aspect ratio materials.[18] Critical to advancing both applied and fundamental aspects of these fields are interfacial nanoparticle assemblies whose mechanical properties can be readily tuned over orders of magnitude.

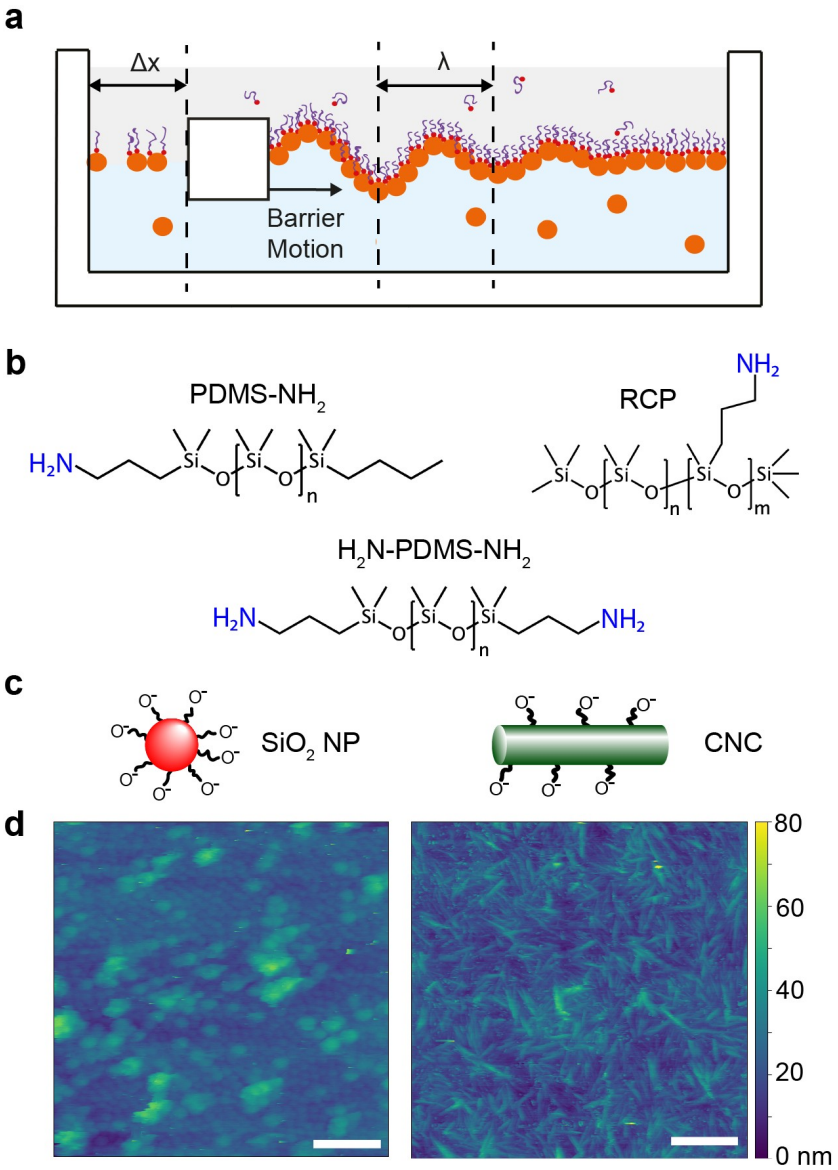

Figure 1 | Nanoparticle surfactants self-assembled at the oil-water interface. a, Schematic of NPS formed at the oil-water interface in a Langmuir trough and the buckling of the assembly in response to confinement by a barrier. **b**, NH_2-functionalized PDMS polymer surfactants dispersed in the non-aqueous phase. **c**, CO_2H-functionalised silica nanoparticles and cellulose nanocrystals

dispersed in the aqueous phase. **d**, *In situ* AFM height topographs of assemblies of 1 mg mL^{-1} SiO_2 NP with 20 mM H_2N-PDMS-NH_2 (scale bar, 100 nm) and 1 mg mL^{-1} CNC with 6 mM RCP (scale bar, 400 nm) at the oil-water interface.

Here, we study the bending moduli of assemblies of NPSs at the oil-water interface. NPS consist of NPs and polymer surfactants that are initially dispersed in separate, immiscible liquids. Provided that the functional groups on the NPs and surfactants are complementary, e.g., ion pairing, the two components bind to one another at the liquid-liquid interface to form NPSs.[19] The resulting NPSs are irreversibly trapped at the interface, unless disassembled by an external stimulus. We used a Langmuir trough to study a silica nanoparticle-based NPS system whose adsorption kinetics and interfacial rheology we have extensively characterized elsewhere (**Figure 1**a).[20] The non-aqueous phase consisted of silicone oil (kinematic viscosity, 5 cSt) and NH_2-functionalised PDMS-based polymer surfactants (Figure 1b). Three different linear, amine-functionalized polymer surfactants were chosen that differ in their number of amine groups. PDMS-NH_2 has one primary amine, H_2N-PDMS-NH_2 is capped on both ends with primary amines, and an amine-functionalized random copolymer ('RCP') has multiple, randomly located amine groups per molecule. The aqueous phase contained 1 mg mL^{-1} of $-CO_2H$-functionalised spherical silica NPs (average radius 7 nm, polydispersity $\lesssim 10\%$, Figure 1c).

In situ liquid-phase atomic force microscopy (AFM) of the NPS assemblies performed using a high-viscosity silicone oil (kinematic viscosity, 60000 cSt) showed disordered, densely packed assemblies of discrete particles (Figure 1d). Typically, AFM topographs showed a narrow range of height variation in the assembly smaller than a particle diameter, indicative of a monolayer of NPSs with a well-defined contact angle (Supplementary Figure 1). In one case (H_2N-PDMS-NH_2, 20 mM, Supplementary Figure 1c) large-scale surface roughness on a length scale of ~100 nm was observed, indicative of aggregation of the particles at the interface. As particle shape anisotropy due to

particle aggregation is known to cause strong capillary interactions between particles,[21] a monolayer-forming control sample comprising NPS assemblies made from rod-like cellulose nanocrystals (CNC) and RCP (6 mM) was also studied. AFM topographs also indicated monolayer formation in the case of the CNC-RCP system (Supplementary Figure 1d). After ageing, extremely small translations of the barrier (of order microns) caused interfacial buckling and the formation of wrinkles. The wavelength of these wrinkles was did not change on the experimental timescale and did not depend on the extent of barrier translation.

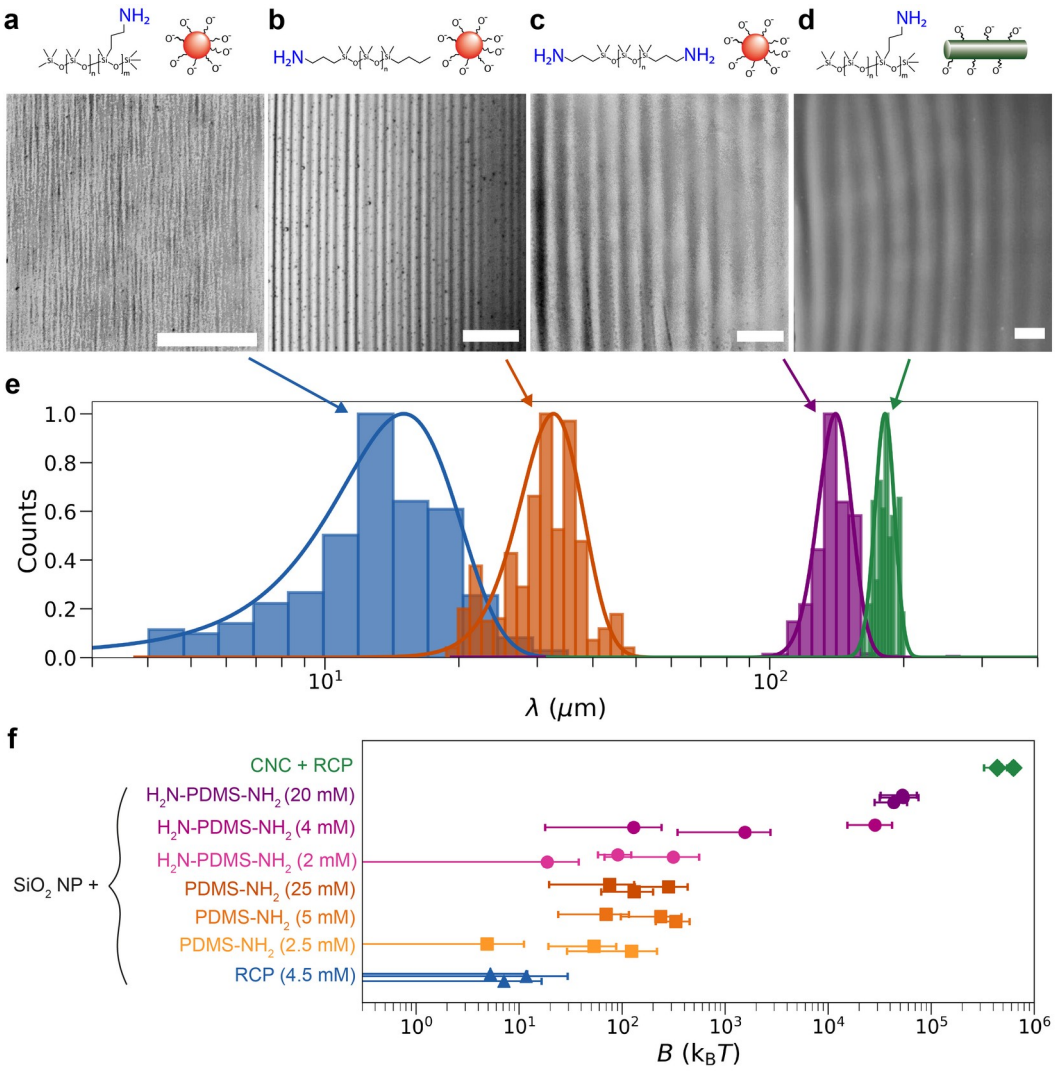

Figure 2 | Buckling of incompressible NPS films in response to confinement. Wrinkles formed by confining NPS assemblies comprising SiO_2 NPs with **a**, RCP (4.5 mM), **b**, PDMS-NH_2 (25mM), **c**, H_2N-PDMS-NH_2 (20 mM), and **d**, CNC with RCP (6 mM). Scale bars, 200 μm. **e**, Normalised histograms of wrinkle wavelengths measured from different assemblies. Arrows indicate system composition, solid lines show Gaussian fits to the histograms. **f**, Bending moduli for all systems studied in this work as inferred from buckling wavelengths. Each data point shows an independent measurement. Error bars show ± 1 standard deviation (see *Methods*).

Translating the barriers of the trough led to the confinement of the NPSs and, hence, a spatially varying out-of-plane displacement of the assembly (**Figure 2**, Supplementary Videos 1–4 show representative data). The shape adopted by the

film in response to confinement is given by the balance between the bending energy of the NPS assembly and the energetic cost of vertically displacing of the liquids.[22] For small confinements, sinusoidal wrinkling patterns are observed, in which a single, energetically favoured wavelength, λ, of the wrinkles is related to the bending modulus, B, of the assembly as:

$$\lambda = 2\pi \left(\frac{B}{\Delta \rho g} \right)^{\frac{1}{4}}. \quad (1)$$

Where $\Delta \rho$ is the density difference between the two liquid phases, and g = 9.8 m s^{-2}.

Observed λvaried from ~3 μm up to ~300 μm, depending on the composition of the NPS studied (Figure 2b). This translates to a range of bending moduli from sub-k_BT up to 10^6 k_BT. The lowest B was found in SiO_2 NP-based systems when using RCP as a ligand, while the largest was ~10^5 k_BT seen at the highest concentrations of H_2N-PDMS-NH_2, for which AFM topographs showed multilayer formation. Larger still was the bending modulus of the CNC + RCP film (~10^6 k_BT). Reproducibility between measurements was generally good despite using multiple particle batches, with some exceptions. At 4 mM H_2N-PDMS-NH_2, an enormous spread in B was observed, from 10^2 k_BT up to 3×10^4 k_BT, suggesting that a transition from a monolayer to a multilayer structure may occur near this concentration. Wrinkling patterns at concentrations of RCP below 4.5 mM were either transient or highly variable, and so not reported. Comparison with literature values is striking. NP assemblies, which lack polymer ligands, at the liquid–fluid interface typically have extremely small mechanical moduli: Ag, Au, and Fe_3O_4 NPs monolayers and trilayers spread at the liquid-air interface have a B of 10 k_BT or less.[23,24] By contrast, B as high as 10^7 k_BT has been reported in NP monolayers that have been processed into free-hanging assemblies or embedded in polymer matrices.[25,26] To our knowledge, intermediate values for B in NP assemblies are not present in the literature. Measured B for lipid bilayers

are typically in the range 10 – 100 $k_B T$ (Ref. 27), while the reported lower bound for thin polymer films is typically of order 10^7-10^8 $k_B T$ (Ref. 28). Judicious choice of ligands and particles in the NPS allow us control over B across this entire range.

This variation in B stands in sharp contrast to the surface shear moduli, G_s, of the NPS assemblies (0.1 – 1 N m^{-1}, ref. 20), demonstrating the enormous mechanical anisotropies of the NPS assemblies. Classical continuum relations predict that $B = \frac{G_s d^2}{6(1-\nu)}$, where ν is the Poisson ratio, overestimating the lower bound of our measured B by as much as 3 orders of magnitude. This anisotropy arises from the differing physical origins of the in-plane and out-of-plane mechanical response. Resistance to shear is due to the energetic costs of deforming the particle assembly at constant surface area. By contrast, resistance to bending in our system appears to derive, at least in part, from the geometric constraints placed on the surface area of the oil-water interface by the incompressible particle assembly. The geometrical model Kralchevsky *et al.* predicts that $B = \frac{3}{8}\gamma\phi r^2 \sin^4\theta$, where γ, ϕ, and θ are the oil-water interfacial tension, areal particle density, and particle contact angle, respectively.[29] This model predicts $B \approx 1-10^5$ $k_B T$ for the particles studied here (Supplementary Figure 2), with the upper range corresponding to the size of the larger CNC particles or the aggregates seen in AFM micrographs of the SiO_2 NP systems. While this model captures much of the range we find in our measurements, it fails to fully capture the size-dependence observed in particles elsewhere in there literature,[24,30] most likely due to the role of particle ligands.[25,31]

This wide range in B allows us to observe further departure from classical buckling by studying the distribution of λ for a given B. Typical analyses of

particle monolayer buckling predict the emergence of a single, energetically favorable mode in response to confinement. In the range of B studied in this work, however, approximately Gaussian distributions of wavelengths were seen (Figure 2e). As B decreases, the width of this distribution increases, and a broad spectrum of buckling modes emerges as B becomes comparable to thermal energies. Defining a buckling spectral width, $\Delta\lambda = \frac{\sigma_\lambda}{\bar{\lambda}}$, where σ_λ and $\bar{\lambda}$ are the standard deviation and mean of the measured wavelengths respectively, it was found that $\Delta\lambda$ obeyed a power law relation with λ (**Figure 3**). Plotting $\Delta\lambda$ as a function of B (Supplementary Figure 3) produces an identical trend. This relation is not a result of the palette of materials or solvents selected for our work, nor is it an artefact of imaging resolution: analysis of high-resolution data from Leahy *et al.*[23] (Au NPs spread at the air-water/ethanol and air/glycerol interface, $B < \text{¿}k_BT$), and Pocivavsek *et al.*[32] (Au NPs spread at the air-water interface, $B \approx k_BT$) produce spectral widths that fall onto the same trendline.

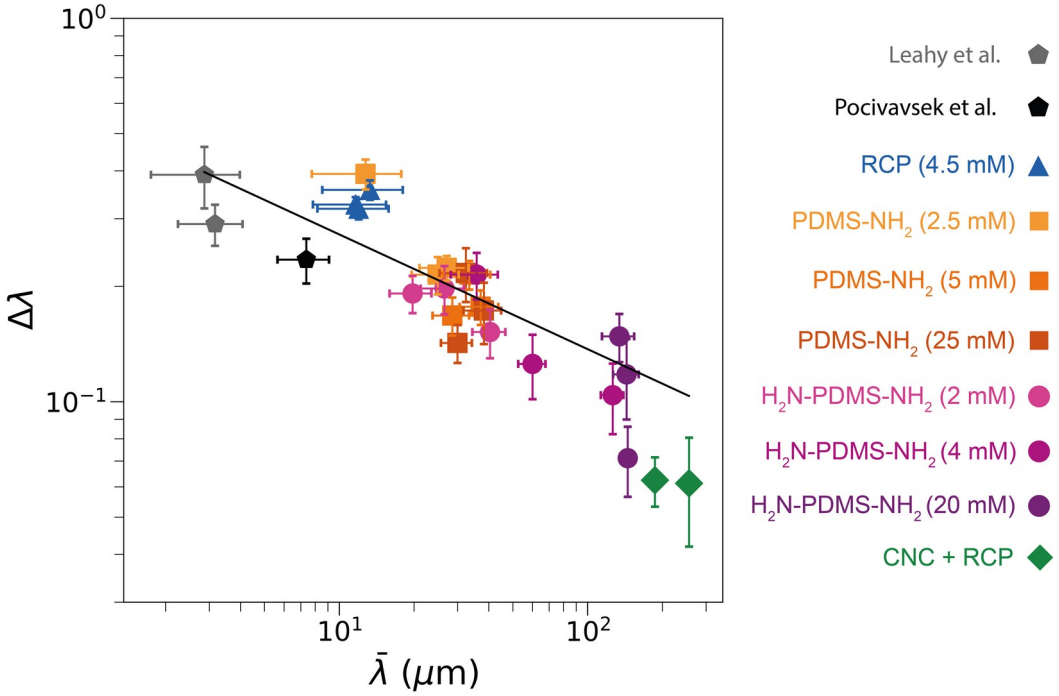

Figure 3 | Power law scaling of buckling spectrum width with buckling wavelength. Fit shows $\Delta\lambda = a\lambda^{-b}$, with $a =$ ¿ 0.5 and $b =$ ¿ 0.3. Color scheme as in Fig. 2, additional data series denoted in legend. Each data point shows an independent measurement. Error bars show ±1 standard deviation (see *Methods*).

Finally, we comment on the confinement field in our trough, which exhibits qualitatively similar behaviour independent of B (**Figure 4**). In all systems studied here, buckling is confined to within a few mm of the barrier that is being translated. Close to this barrier, stresses in the system are concentrated into highly curved folds. Moving away from the barrier, there exists a narrow region of length $\sim\lambda$, where the film transitions from folds to sinusoidal wrinkles. Beyond this, the amplitude of the wrinkles slowly decays (greater variations in gray value correspond to larger wrinkle amplitude). Far from the translating barrier, the assembly is planar. Both the increasing amplitude of the wrinkles and the transition from wrinkles to folds, which occurs in response to increasing confinement, demonstrate that the effective degree of confinement of the film decays with increasing distance from the barrier.

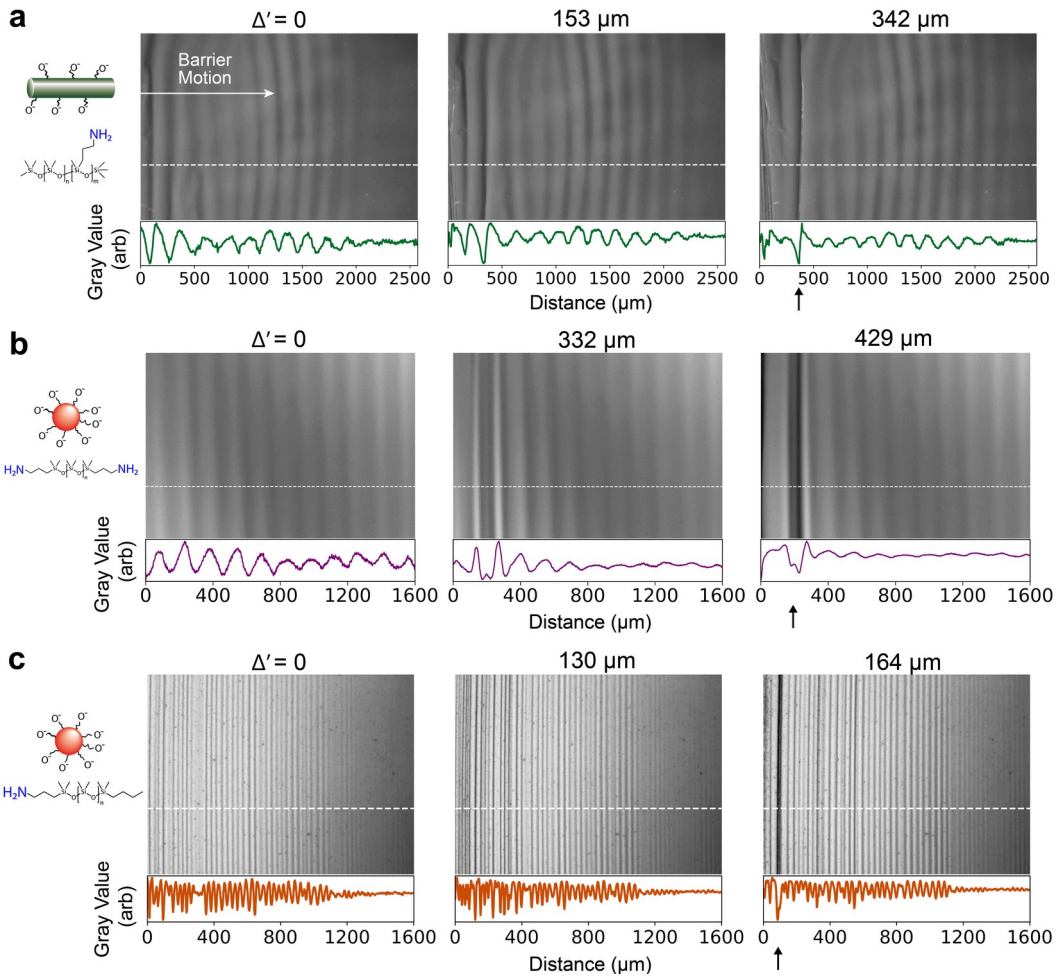

Figure 4 | Coexistence of wrinkles and folds in NPS assemblies. Light micrographs of nanoparticle surfactant assemblies under increasing confinement, Δ'. Plots show gray-scale values after polynomial background subtraction. Note that the barrier was translated prior to experiment to produce wrinkles, and Δ' refers to further translations of the barrier. Grayscale values measured in the region indicated by the white dashed line. Arrows indicate the location of a localized transition from a wrinkle to a fold. **a**, 6 mM RCP, 1 mg mL^{-1} CNC. **b**, 20 mM H_2N-PDMS-NH_2, 1 mg mL^{-1} SiO_2 NP. **c**, 25 mM PDMS-NH_2, 1 mg mL^{-1} SiO_2 NP.

This spatial decay in the degree of confinement is due to pinning of the NPS assembly at the edge of the trough. We confirmed this by imaging the CNC–RCP assembly (which had the largest λ) in dodecane, increasing the refractive

index mismatch between the solvents and allowing us to obtain clear images of the system under reflection imaging without altering B (Supplementary Figure 4). We clearly observed contact line pinning and large hysteresis effects at the edge of the trough upon reversing the applied confinement (Supplementary Videos 5 and 6). It is important to note that the physical origin of these decays is different from that observed by Cicuta *et al*, which was attributed to frictional interactions of a spread monolayer of granular particles with the edges of the trough.[33] In our case, NPS assemblies form a network that spans the trough and are pinned at the wall of the trough. Conservatively taking the roughness of the wall, λ_r, to be of order 0.1–1.0 μm, we estimate that the three-phase contact line is pinned by capillary energies of order $\Delta E \sim \gamma \lambda_r^2 \approx 10^3 - 10^7$ $k_B T$, providing a significant barrier to relaxation of the folds into wrinkles.

Our results have their most immediate applications in microfluidics and reconfigurable, droplet-based materials. The enhanced bending moduli of the assemblies presented here are critical in balancing the overpressure produced by flows in all-liquid microfluidic platforms,[34] as well as in preventing structural failure due to Ostwald ripening.[35] In printed cellular materials, as well as droplet-based constructs, *in situ* alteration of interfacial bending moduli could be used to drive shape changes and actuation.[36] Interfaces with tunable rigidity open the possibility of complex shape transformations in droplets containing synthetic cytoskeletons.[37] Finally, our findings motivate the need for new theoretical tools that describe the buckling of extremely thin materials made of discrete objects. Descriptions of homogeneous thin films buckling with multiple modes exist, but do not capture the phenomena we observe here.[38] It may be that models that account for the discrete nature of the NPs are more successful in describing the mechanical properties of our assemblies.[39]

Acknowledgments

This work was supported by the U.S. Department of Energy, Office of Science, Office of Basic Energy Sciences, Materials Sciences and Engineering Division under Contract No. DE-AC02-05-CH11231 within the Adaptive Interfacial Assemblies Towards Structuring Liquids program (KCTR16). Portions of the work—including the AFM imaging—were carried out as a User Project at the Molecular Foundry, which is supported under the same contract.

References

1. Tian, X. *et al.* On the shuttling across the blood-brain barrier via tubules formation: mechanism and cargo avidity bias. *Sci. Adv.* **6**, eabc4397 (2020).
2. Simunovic, M., Prévost, C., Andrew, C. J. & Bassereau, P. Physical basis of some membrane shaping mechanisms. *Philos. Trans. R. Soc. A Math. Phys. Eng. Sci.* **374**, (2016).
3. Haas, P. A., Höhn, S. S. M. H., Honerkamp-Smith, A. R., Kirkegaard, J. B. & Goldstein, R. E. *The noisy basis of morphogenesis: Mechanisms and mechanics of cell sheet folding inferred from developmental variability*. *PLoS Biology* **16**, (2018).
4. Ku, K. H., Li, J., Yoshinaga, K. & Swager, T. M. Dynamically Reconfigurable, Multifunctional Emulsions with Controllable Structure and Movement. *Adv. Mater.* **31**, 1–8 (2019).
5. Nagelberg, S. *et al.* Reconfigurable and responsive droplet-based compound micro-lenses. *Nat. Commun.* **8**, 1–9 (2017).
6. Yang, Z., Wei, J., Sobolev, Y. I. & Grzybowski, B. A. Systems of mechanized and reactive droplets powered by multi-responsive

surfactants. *Nature* **553**, 313–318 (2018).

7. Forth, J. *et al.* Building Reconfigurable Devices Using Complex Liquid–Fluid Interfaces. *Adv. Mater.* 1806370 (2019). doi:10.1002/adma.201806370
8. Dong, A., Chen, J., Vora, P. M., Kikkawa, J. M. & Murray, C. B. Binary nanocrystal superlattice membranes self-assembled at the liquid-air interface. *Nature* **466**, 474–477 (2010).
9. Stratford, K., Adhikari, R., Pagonabarraga, I., Desplat, J.-C. & Cates, M. E. Colloidal jamming at interfaces: a route to fluid-bicontinuous gels. *Science* **309**, 2198–2201 (2005).
10. Herzig, E. M., White, K. A., Schofield, A. B., Poon, W. C. K. & Clegg, P. S. Bicontinuous emulsions stabilized solely by colloidal particles. *Nat. Mater.* **6**, 966–971 (2007).
11. Forth, J. *et al.* Reconfigurable Printed Liquids. *Adv. Mater.* **30**, 1707603 (2018).
12. Villar, G., Heron, A. J. & Bayley, H. Formation of droplet networks that function in aqueous environments. *Nat. Nanotechnol.* **6**, 803–808 (2011).
13. Zhou, L. *et al.* Lipid-Bilayer-Supported 3D Printing of Human Cerebral Cortex Cells Reveals Developmental Interactions. *Adv. Mater.* **32**, (2020).
14. Feng, W. *et al.* Harnessing liquid-in-liquid printing and micropatterned substrates to fabricate 3-dimensional all-liquid fluidic devices. *Nat. Commun.* **10**, 1095 (2019).
15. Rodríguez-Arco, L., Li, M. & Mann, S. Phagocytosis-inspired behaviour in synthetic protocell communities of compartmentalized colloidal objects. *Nat. Mater.* **16**, 857–863 (2017).
16. Alt, S., Ganguly, P. & Salbreux, G. Vertex models: From cell mechanics to tissue morphogenesis. *Philos. Trans. R. Soc. B Biol. Sci.* **372**, (2017).

17. Villar, G., Graham, A. D. & Bayley, H. A Tissue-Like Printed Material. *Science (80-.).* **340**, 48–52 (2013).
18. Davidovitch, B., Schroll, R. D., Vella, D., Adda-Bedia, M. & Cerda, E. a. Prototypical model for tensional wrinkling in thin sheets. *Proc. Natl. Acad. Sci. U. S. A.* **108**, 18227–32 (2011).
19. Cui, M., Emrick, T. & Russell, T. P. Stabilizing liquid drops in nonequilibrium shapes by the interfacial jamming of nanoparticles. *Science (80-.).* **342**, 460–464 (2013).
20. Toor, A. *et al.* Mechanical Properties of Solidifying Assemblies of Nanoparticle Surfactants at the Oil–Water Interface. *Langmuir* **35**, 13340–13350 (2019).
21. Lewandowski, E. P. *et al.* Orientation and self-assembly of cylindrical particles by anisotropic capillary interactions. *Langmuir* **26**, 15142–15154 (2010).
22. Zhang, Q. & Witten, T. A. Microscopic wrinkles on supported surfactant monolayers. *Phys. Rev. E - Stat. Nonlinear, Soft Matter Phys.* **76**, 1–11 (2007).
23. Leahy, B. D. *et al.* Geometric stability and elastic response of a supported nanoparticle film. *Phys. Rev. Lett.* **105**, (2010).
24. You, S. S. *et al.* Comparison of the mechanical properties of self-assembled Langmuir monolayers of nanoparticles and phospholipids. *Langmuir* **29**, 11751–11757 (2013).
25. Mueggenburg, K. E., Lin, X.-M., Goldsmith, R. H. & Jaeger, H. M. Elastic membranes of close-packed nanoparticle arrays. *Nat. Mater.* **6**, 656–660 (2007).
26. Gu, X. W. *et al.* Tolerance to structural disorder and tunable mechanical behavior in self-assembled superlattices of polymer-grafted nanocrystals.

Proc. Natl. Acad. Sci. **114**, 2836–2841 (2017).

27. Elani, Y. *et al.* Measurements of the effect of membrane asymmetry on the mechanical properties of lipid bilayers. *Chem. Commun.* **51**, 6976–6979 (2015).
28. Huang, J., Davidovitch, B., Santangelo, C. D., Russell, T. P. & Menon, N. Smooth cascade of wrinkles at the edge of a floating elastic film. *Phys. Rev. Lett.* **105**, 2–5 (2010).
29. Kralchevsky, P. A., Ivanov, I. B., Ananthapadmanabhan, K. P. & Lips, A. On the thermodynamics of particle-stabilized emulsions: Curvature effects and catastrophic phase inversion. *Langmuir* **21**, 50–63 (2005).
30. Horozov, T. S., Binks, B. P., Aveyard, R. & Clint, J. H. Effect of particle hydrophobicity on the formation and collapse of fumed silica particle monolayers at the oil-water interface. *Colloids Surfaces A Physicochem. Eng. Asp.* **282**–**283**, 377–386 (2006).
31. Griesemer, S. D. *et al.* The role of ligands in the mechanical properties of Langmuir nanoparticle films. *Soft Matter* **13**, 3125–3133 (2017).
32. Pocivavsek, L. *et al.* Stress and Fold Localization in Thin Elastic Membranes. *Science (80-.).* **320**, 912–916 (2008).
33. Cicuta, P. & Vella, D. Granular character of particle rafts. *Phys. Rev. Lett.* **102**, 1–4 (2009).
34. Vitantonio, G. Di, Wang, T., Haase, M. F., Stebe, K. J. & Lee, D. Robust Bijels for Reactive Separation via Silica-Reinforced Nanoparticle Layers. *ACS Nano* **13**, 26–31 (2019).
35. Abkarian, M. *et al.* Dissolution arrest and stability of particle-covered bubbles. *Phys. Rev. Lett.* **99**, 1–4 (2007).
36. Santa Chalarca, C. F., Letteri, R. A., Perazzo, A., Stone, H. A. & Emrick, T. Building Supracolloidal Fibers from Zwitterion-Stabilized Adhesive

Emulsions. *Adv. Funct. Mater.* **28**, 1–10 (2018).

37. Caggioni, M., Lenis, J., Bayles, A. V, Furst, E. M. & Spicer, P. T. Temperature-Induced Collapse, and Arrested Collapse, of Anisotropic Endoskeleton Droplets. *Langmuir* **31**, 8558–8565 (2015).
38. Matoz-Fernandez, D. A., Davidson, F. A., Stanley-Wall, N. R. & Sknepnek, R. Wrinkle patterns in active viscoelastic thin sheets. *Phys. Rev. Res.* **2**, 013165 (2020).
39. Tordesillas, A., Carey, D., Croll, A. B., Shi, J. & Gurmessa, B. Micromechanics of elastic buckling of a colloidal polymer layer on a soft substrate: experiment and theory. *Granul. Matter* **16**, 249–258 (2014).

Extended Experimental Section

Materials

Carboxylic acid-functionalized cellulose nanocrystals ($r = 5-10$nm, length, $l = 100-150$nm) were obtained from Blue Goose Biorefineries (Saskatchewan, Canada) and used as received. Carboxylic acid-functionalized silica NPs (average radius, r = 7 nm, polydispersity, $\frac{\sigma_r}{r} \lesssim 0.1$, where σ_r is the standard deviation in the particle size distribution) were obtained from Microspheres Nanospheres and purified by dialysis against deionized water (dialysis membrane molecular weight cut-off, 12–14 kg mol^{-1}) for 2 days. To generate particle-saturated interfaces, as well as to improve system reproducibility due to pH-sensitive surface activity, particles were diluted to the required concentration in a 2-(*N*-morpholino)ethanesulfonic acid buffer (MES, 5 mM). pH of the buffer was adjusted to 6.4 using 1 M solutions of HCl or NaOH. Monoaminopropyl terminated poly(dimethylsiloxane) (PDMS-NH_2, M_w = 1.75 kg mol^{-1}) was purchased from Gelest Inc. and used as received. Poly[dimethylsiloxane-*co*-(3-

aminopropyl)methylsiloxane] (RCP, $M_w \approx 11$ kg mol^{-1}, estimated using the relation for linear siloxane polymers in Kataoka and Ueda[40]) and bis(3-aminopropyl) terminated poly(dimethylsiloxane) (H_2N-PDMS-NH_2, $M_w = 2.5$ kg mol^{-1}) were purchased from Sigma Aldrich and used as received.

Trough Design and Operation. NPS assemblies were formed in a CNC-milled Delrin Langmuir trough with an oil-water interface contact area of dimensions 3 × 8 cm. A circular hole in the bottom of the trough, which enabled transmission imaging, was covered with a circular borosilicate glass cover slip (diameter, 22 mm) and sealed with Norland Optical Adhesive 61 that was exposed to UV light and left to fully cure for 24 h prior to experimentation. The barriers were moved manually using a linear translation stage and imaged under transmission illumination unless stated otherwise.

NPS Assembly and Data Analysis. A planar oil–water interface was produced using a trough with a lip that pinned the oil–water interface. This allowed the contact angle at the three-phase contact line to be varied simply by varying the volume of aqueous phase. Planarity of the interface was achieved by shining a light on to the air–water interface and adjusting the volume of the aqueous phase until a specular reflection was produced, after which the non-aqueous phase was gently pipetted on top of the aqueous phase. Films were aged for up to 3 h prior to compression, with ageing times determined from the saturation times of rheological moduli in the case of SiO_2 NP measurements,[20] or empirically for the CNC-RCP system. Preliminary image processing was performed using FIJI, high-throughput measurements of wrinkle wavelength were performed using Python, *numpy,* and *scikit-image*.[41–43]

In situ AFM microscopy. *In situ* liquid phase AFM microscopy was performed using the method more fully described in Chai *et al.*[44] Briefly, polymer surfactants were dispersed for 48 h at 60 ˚C in a high viscosity silicone oil (kinematic viscosity, 60000 cSt). The non-aqueous phase was formed by dropping the solution onto a silicon substrate, which was then vacuum dried for 10 min. 40 μL of aqueous NP dispersion was then used to form a water bridge between the sample and the tip holder. All samples were equilibrated for 30 min to allow for film assembly prior to imaging. AFM micrographs were obtained using a Cypher ES AFM.

Estimation of Errors. The error in the bending modulus, σ_B, shown in Figure 2e, was calculated using standard error propagation relations for Equation 1, yielding:

$$\frac{\sigma_B}{B} = \frac{4\sigma_\lambda}{\lambda'}.$$

Where λ' and σ_λ are the mean and standard deviation in the measured distributions of observed wavelengths. Errors in σ_λ were estimated *via* bootstrapping using sampling by replacement as implemented in *scikit-learn*.[45] Error bars in Figure 3 show the standard deviation in 10000 sampled distributions.

References (Methods Section)

40. Kataoka, T. & Ueda, S. Viscosity-Molecular Weight Relationship for Polydimethylsiloxane. *Polym. Lett.* **4**, 317–322 (1966).
41. Schindelin, J. *et al.* Fiji: An open-source platform for biological-image analysis. *Nat. Methods* **9**, 676–682 (2012).
42. Harris, C. R. *et al.* Array programming with NumPy. *Nature* **585**, 357–362 (2020).

43. van der Walt, S. *et al.* scikit-image: image processing in Python. *PeerJ* **2**, e453 (2014).

44. Chai, Y., Lukito, A., Jiang, Y., Ashby, P. D. & Russell, T. P. Fine-Tuning Nanoparticle Packing at Water–Oil Interfaces Using Ionic Strength. *Nano Lett.* **17**, acs.nanolett.7b03462 (2017).

45. Pedregosa, F. *et al.* Scikit-learn: Machine Learning in Python. *J. Mach. Learn. Res.* **12**, 2825–2830 (2011).